Optics Letters

Controlling X-ray emission with dispersion-engineered surface plasmon polaritons

H. Aknin,[1,*] Y. Klein,[1,2] and S. Shwartz[1,3]

[1] Physics Department and Institute of Nanotechnology, Bar-Ilan University, Ramat Gan, 52900, Israel
[2] Department of Physics, University of Ottawa, Ottawa, Ontario K1N 6N5, Canada
[3] Sharon.shwarz@biu.ac.il
*akninha@biu.ac.il

Received 28 January 2026; revised 5 March 2026; accepted 5 March 2026; posted 13 March 2026; published 27 March 2026

We propose controlling the angular and spectral distribution of hard x-ray emission by entangling x-ray photons with ultraviolet surface plasmon polaritons (SPPs) whose dispersion is engineered by a metal-dielectric multilayer on a nonlinear crystal. Spontaneous parametric down-conversion of an x-ray pump produces a hard x-ray signal photon correlated with an ultraviolet SPP mode near its resonance. Engineering the SPPs dispersion reshapes the phase-matching landscape and imprints tunable angular-spectral structure on the emitted x-ray photons. The scheme enables compact, designable control of x-ray emission and extends surface-plasmon-assisted nonlinear x-ray optics.

https://doi.org/10.1364/OL.591904

Controlling the propagation direction and spectrum of electromagnetic radiation is central to modern science and technology, underpinning applications ranging from precision sensing to information processing and communication [1]. At optical frequencies, such control is routinely achieved by engineering light–matter interactions mediated by valence electrons, for example, using dispersion engineering, nonlinear optical processes, and plasmonic confinement [2]. In the hard x-ray regime, however, the large photon energy and momentum render the coupling to valence electrons intrinsically weak, leaving most materials with refractive indices close to unity and severely limiting the degrees of freedom available for shaping x-ray radiation.

Recently, we experimentally demonstrated control over the emission direction and spectrum of hard x-rays by entangling x-ray photons with ultraviolet surface plasmon polaritons (SPPs) [3]. In that work, the entanglement was generated via spontaneous parametric down-conversion (SPDC) of an x-ray pump into an x-ray signal photon and a near-field ultraviolet SPP at the surface of an aluminum crystal. Because the signal is born entangled with the SPP, energy and transverse-momentum conservation map the SPP dispersion onto the angular-spectral distribution of the emitted x-rays. The accessible tuning range in that proof-of-principle experiment, however, was largely set by the intrinsic material response, leaving only limited control via the choice of crystal or the dielectric environment.

Here, we extend this concept by introducing a dispersion-engineered metal-dielectric multilayer stack that tailors the ultraviolet SPP dispersion. This added design freedom enables deterministic and reconfigurable control over the x-ray emission directionality and spectrum, without modifying the underlying nonlinear crystal.

We note that a recent theoretical study proposed a related route to controlling x-ray emission by exploiting x-ray to optical SPDC in nonlinear photonic crystals, where photonic dispersion is engineered to shape the generated radiation [4]. In contrast, we shape the x-ray emission by engineering the dispersion of a surface-bound plasmonic partner, rather than a propagating optical photon, enabling control through near-field confinement at a metal interface. More broadly, several experiments over the past decade have demonstrated nonlinear wave-mixing processes that couple hard x-rays to longer-wavelength fields [5–12]. While the conversion efficiencies in this regime remain low, they are nevertheless measurable and sufficient to reveal rich physics.

We consider an x-ray emission control scheme as is illustrated in Fig. 1. The structure comprises a stack of thin non-crystalline aluminum (Al)-alumina (Al_2O_3) bilayers on the top of an Al crystal. This structure is illuminated by a monochromatic, plane wave x-ray pump at frequency $\omega_{p,0}$ and incident angle θ_p, generating signal and idler photons at ω_s and ω_i through nonlinear interaction in the crystal. The signal photon is emitted close to the Bragg direction and is parameterized by small angular deviations: an in-scattering-plane deviation $\delta\theta_s$ relative to the Bragg angle, and an out-of-scattering-plane deviation $\delta\phi_s$, relative to the x-z plane.

When the frequency of the idler photon matches the surface plasmon resonance (SPR) frequency and its in-plane momentum matches that of the SPP mode, strong coupling occurs, and the idler forms an SPP [3]. Through conservation laws, the multilayer-controlled SPP dispersion is directly imprinted onto the angular distribution and spectrum of the generated entangled x-ray signal photon [3]. The x-ray emission is therefore dictated by the generalized SPP dispersion relation of the multilayer.

To model SPDC in a lossy dispersive medium, we use macroscopic quantum electrodynamics (MQED), which quantizes the macroscopic Maxwell equations for the electric-field operators

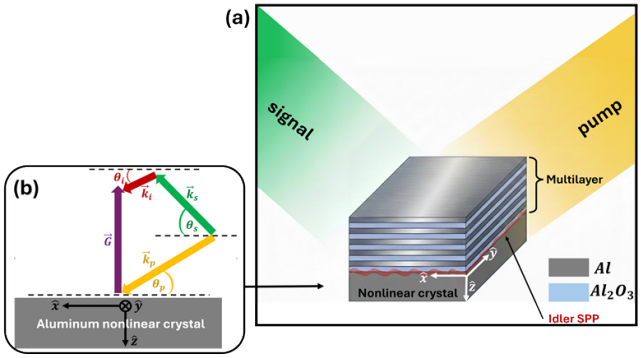

Fig. 1. (a) Schematic of x-ray-to-SPP SPDC with dispersion engineering. A monochromatic x-ray pump beam impinges on an aluminum nonlinear crystal at incidence angle θ_p, generating an x-ray signal photon and an idler excitation that couples to a dispersion-engineered SPP at the metal-dielectric interface. (b) Phase-matching diagram, showing the k-vectors of the pump, signal, and idler, kp, ks, and ki, and the reciprocal-lattice vector G (purple). Angles are defined with respect to the atomic planes (dashed lines).

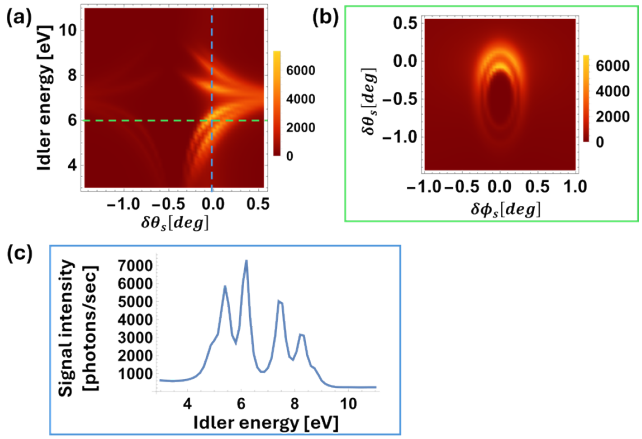

Fig. 2. (a) Simulated signal intensity as a function of the detector angle and idler photon energy for a metal-dielectric multilayer comprising three Al layers separated by Al_2O_3, with an identical thickness of $d_{Al} = d_{Al_2O_3} = 7$ nm. (b) Signal angular spectrum for $\hbar\omega_i = 6$ eV, corresponding to the green dashed line in (a). (c) Signal energy spectrum for $\delta\theta_s = -0.02°$ corresponding to the blue dashed line in (a).

in absorbing media [13,14]. Dissipation is incorporated via a Langevin formulation by introducing noise current operators, $\hat{j}_N$. Together with the nonlinear current operators, $\hat{j}_{NL}$, the total source current driving the field at the u^{th} mode is given by $\hat{j}_u = \hat{j}_{NL,u} + \hat{j}_{N,u}$, where $u = s, i$ denote the signal and idler modes, respectively [3,13,14].

For the present geometry, which exhibits translation symmetry in the transverse plane $\vec{\rho} = (x, y)$, we Fourier transform the electric field and current density as $\hat{E}(\vec{r}, \omega) = \int \frac{d^2q}{(2\pi)^2} e^{i\vec{q}\cdot\vec{\rho}} \hat{E}(q, \omega, z)$ and $\hat{J}(\vec{r}, \omega) = \int \frac{d^2q}{(2\pi)^2} e^{i\vec{q}\cdot\vec{\rho}} \hat{J}(q, \omega, z)$, where $\vec{q} = (q_x, q_y)$ is the transverse wavevector. The Maxwell wave equation for the signal and idler electric-field operators in the nonlinear crystal then becomes [3]:

$$\left(\partial_z\hat{z} + i\vec{q}_u\right) \times \left(\partial_z\hat{z} + i\vec{q}_u\right) \times \hat{E}_u(q_u, \omega_u, z) - \frac{\omega_u^2}{c^2} \varepsilon(z, \omega_u) \hat{E}_u(q_u, \omega_u, z) = -i\omega_u \mu_0 \hat{J}_u(q_u, \omega_u, z), \quad (1)$$

where $\varepsilon(z, \omega_u)$ is the position dependent permittivity.

To solve the wave equation for the electric-field operators, we note that the penetration depth of the idler in the Al nonlinear crystal is much shorter than its wavelength. Consequently, at the idler frequency, the nonlinear current density is much smaller than the Langevin noise current, $\hat{j}_{NLi} \ll \hat{j}_{Ni}$ [3]. In this limit, the idler field is dominated by vacuum fluctuations, and its correlation function is determined by the imaginary part of the electromagnetic Green's tensor, $g_{q_i}(z, z', \omega_i)$, defined by the Maxwell equation for $\hat{E}_i$ [3].

This approximation decouples the signal and idler equations, since the nonlinear mixing contribution to the idler field is negligible. We therefore solve first for $\hat{E}_i$ and then substitute it into the signal-field equation to obtain $\hat{E}_s$.

The x-ray signal count rate, Γ_s, is calculated using the standard photon number operator in the Heisenberg picture, $\Gamma_s = \langle 0|\hat{a}_s^\dagger \hat{a}_s|0\rangle$, where $\hat{a}_s^\dagger$ and $\hat{a}_s$ are the creation and annihilation operators for the signal mode at the output of the crystal and are related to the signal electric-field operators $\hat{E}_s$ by: $\hat{E}_s(q_s, \omega_s, z) = \sqrt{\frac{2\hbar\omega_s\eta(\omega_s)}{\sin(\theta_s)}} \hat{a}_s(q_s, \omega_s, z)$, where $\eta(\omega_s)$ is the impedance of the signal field [3].

The count rate of the x-ray signal photons is given by [3]:

$$\Gamma_s = \int d\omega_i \int \frac{d^2q_s}{(2\pi)^2} \frac{\hbar\omega_i^2}{\pi\epsilon_0 c^2} \left|C(q_s, q_p, \omega_i)\right|^2 \frac{q_i^2}{k_i^2(\omega_i)} \times \int_L^0 dz' \int_L^0 dz e^{i\Delta k_{p,s}(z-z')} \mathrm{Im}\left\{g_{q_i}^{(z,z)}(z, z', \omega_i)\right\}, \quad (2)$$

where L is the thickness of the nonlinear crystal. The integration ranges of the idler frequency ω_i and the signal transverse wave vector $\vec{q}_s$ are set by the energy bandwidth and the angular acceptance of the detector. We note that the momentum conservation at the surface of the nonlinear crystal imposes $\vec{q}_i = \vec{q}_p - \vec{q}_s$. Since the pump is a monochromatic plane wave, the integration in Eq. (2) is performed only over q_s, and no independent integration over q_i. The scalar Green's function $g_{q_i}^{(z,z)}$ is the (z,z) component of the Green's tensor, g_{q_i}. For a planar interface at $z = 0$, it contains a bulk term and a reflected term determined by the multilayer reflection coefficient (see Supplement 1). Consequently, the properties of the bilayer structure and its materials enter the signal count rate through g_{q_i} [3]. The longitudinal phase mismatch is $\Delta k_{p,s} = k_{p,z}(q_p, \omega_{p,0}) + k_{s,z}(q_s, \omega_{p,0} - \omega_i) - G$, where $k_{p,z}$ and $k_{s,z}$ are the longitudinal pump and signal wave vectors, respectively, and G is the reciprocal-lattice vector used for phase matching. The idler contribution to the longitudinal phase mismatch is included implicitly via the exponential part of $g_{q_i}^{(z,z)}$ which depends on the longitudinal idler k-vector, $k_{i,z}$ (see Supplement 1). The prefactor $C(q_s, q_p, \omega_i)$ is given by $C(q_s, q_p, \omega_i) = -\frac{\mu_0\omega_s|\vec{G}\|\vec{E}_{p,0}|\sigma(\omega_s,\omega_i)(\hat{e}_s\cdot\hat{e}_p)}{2k_{s,z}(q_s,\omega_s)} \sqrt{\frac{\omega_s \sin(\theta_s)}{2\hbar\eta(\omega_s)}}$ where $|\vec{E}_{p,0}|$ is the amplitude of the monochromatic plane wave pump electric field, $\omega_s = \omega_{p,0} - \omega_i$ and $\sigma(\omega_s, \omega_i)$is given by $\sigma(\omega_s, \omega_i) = \frac{e^2\rho_G}{m^2\omega_{p,0}\omega_i^2\omega_s} \ll 1$ is the nonlinear coefficient with ρ_G the G-th Fourier component of the unperturbed charge density, ρ_0, given by: $\rho_G = \frac{1}{V}\int_V \rho_0 e^{-i\vec{G}\cdot\vec{r}} d^3r$, where the integration is performed over the volume, V, of the unit cell [3,15].

Next, we consider the following parameters in our simulation: we assumed the nonlinear crystal is illuminated with a pump beam of energy $\hbar\omega_p = 10KeV$ and a flux of $2\times10^{12}\left[\frac{photons}{sec}\right]$

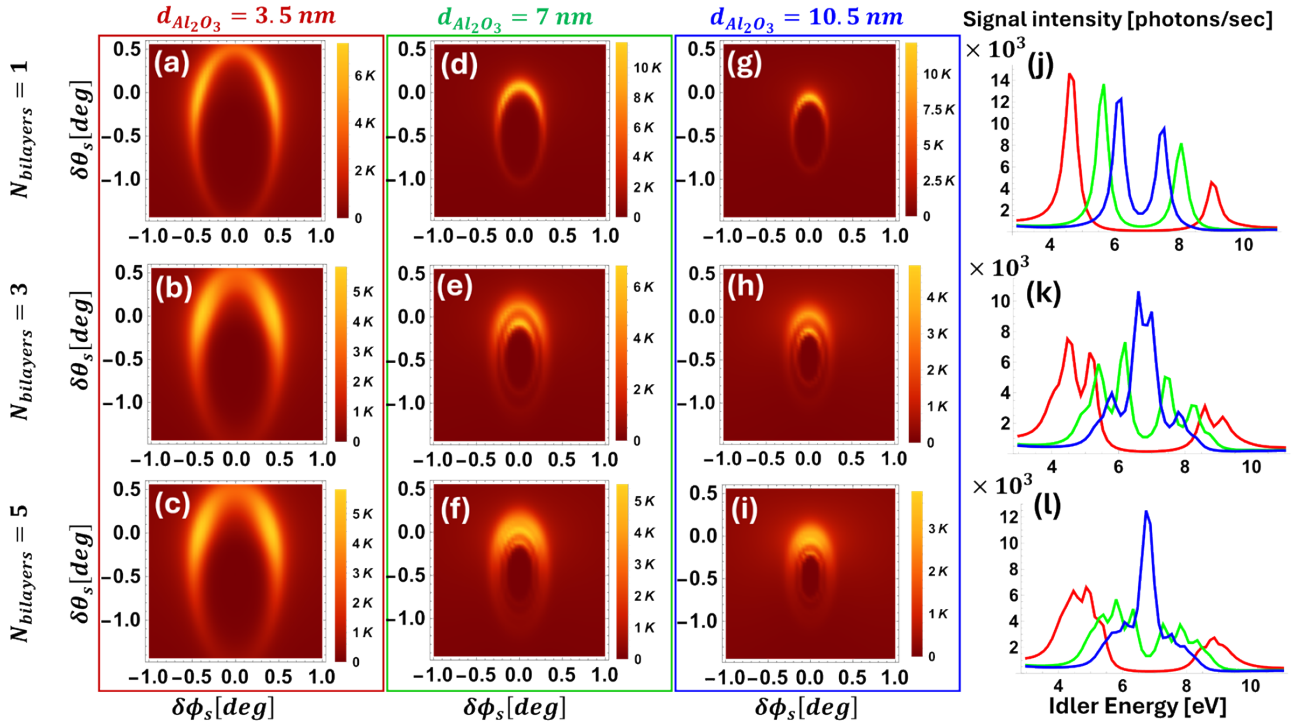

Fig. 3. Signal angular spectrum at $\hbar\omega_i = 6$ eV for three $d_{Al_2O_3}$ thicknesses: (a)–(c): $d_{Al_2O_3} = 3.5$ nm, (d)–(f): $d_{Al_2O_3} = 7$ nm and (g)–(i): $d_{Al_2O_3} = 10.5$ nm. Signal energy spectrum for $\delta\theta_s = -0.02°$ and $\delta\phi_s = 0$ is shown in (j)–(l). In all panels, the number of bilayers is 1 (top row), 3 (middle row), and 5 (bottom row).

and that phase matching is achieved using the reciprocal-lattice vector normal to the Al (0,2,2) planes.

We first illustrate how our scheme with these parameters controls the emission of the signal x-ray field. Fig. 2(a) shows the signal intensity as a function of detector angle and idler energy. A prominent feature is the band-like dispersion of the x-ray signal photons. This structure arises from the plasmonic multilayer, which reshapes the joint signal-idler phase-matching landscape.

In Fig. 2(b), we show the angular distribution of the x-ray signal photons in the $(\delta\theta_s, \delta\phi_s)$ plane, evaluated for signal photons selected along the green dashed trajectory in Fig. 2(a) and centered at $\hbar\omega_s = \hbar\omega_p - 6$ eV (corresponding to an idler energy of 6 eV). Of importance, this angular distribution is energy dependent. By selecting a different signal energy (corresponding to shifting the green dashed line in Fig. 2(a) to up or down), we can modify the angular distribution of the emitted x-ray signal.

Figure 2(c) presents the corresponding spectral shaping. We plot the signal intensity as a function of idler energy $\hbar\omega_i$ for signal photons emitted along the blue dashed trajectory in Fig. 2(a), centered at $\delta\theta_s = -0.02°$ and $\delta\phi_s = 0$. The trajectory at $\delta\phi_s = 0°$ and $\delta\theta_s \approx 0°$ is selected because it maximizes the emission throughput while preserving clear spectral separation of the resonances. Moving to negative $\delta\theta_s$ reduces the signal intensity, whereas positive $\delta\theta_s$ leads to partial spectral overlap. As is evident from Fig. 2(a), selecting a different angular trajectory (corresponding to shifting the blue dashed line in Fig. 2(a) to the left or to the right) leads to a different emission spectrum. In addition, distinct regions of strongly suppressed emission are evident across the angle-energy maps. These correspond to plasmonic bandgaps, i.e., parameter ranges in which no allowed idler SPP mode exists in the multilayer, thereby "blocking" SPDC emission into the corresponding signal angles and energies. In this way, the multilayer functions as a combined angular and spectral filter with near-unity extinction in selected regions of phase space. Additional control is achieved by varying the number of bilayers. Figure 3 presents the emission angles and idler energies for several bilayer thicknesses. It is prominent that varying the number of bilayers primarily controls the modal multiplicity. As $N_{bilayers}$ increases from 1 to 3 to 5, additional rings appear in the signal angular spectra [Figs. 3(a–i)], reflecting the emergence of additional dispersion branches. Consistently, additional resonances appear in the energy spectra. Increasing $d_{Al_2O_3}$ reduces the characteristic scattering-angle radius in Figs. 3(a–i). Spectrally, the low-energy resonances blue-shift and weaken, while higher-energy resonances red-shift and strengthen as they approach $\hbar\omega_i = 7$ eV, the SPR of a single Al/Al_2O interface. The net effect is a tighter clustering of both angular and spectral features. This trend can be understood by considering the limit $d_{Al_2O_3} \to \infty$, where the scheme effectively reduces to a single Al/Al_2O interface and supports a single SPP branch. That branch exhibits the smallest in-plane scattering-angle radius over the full idler-energy range and an SPR energy near 7 eV. Accordingly, as $d_{Al_2O_3}$ increases, the multilayer branches converge toward the single-interface SPP dispersion. Finally, Fig. 3 demonstrates that the multilayer can be engineered to enhance or suppress the signal. For example, with five bilayers the signal count rate at 7 eV increases by a factor of 127 by changing the dielectric layers' thickness from 3.5 nm to 10.5 nm.

Although demonstrated for the Al/Al_2O_3 multilayer platform, the underlying control mechanism is general. It relies on two requirements: the presence of a nonlinear medium supporting x-ray SPDC and a plasmonic structure sustaining a confined

SPP mode at the idler frequency. The theoretical framework employed here, based on Green's tensor electrodynamics and dispersion-engineered phase matching, can therefore be applied to a broad class of plasmonic-nonlinear multilayer systems. In particular, noble metals such as gold or silver, which support low-loss SPPs at visible wavelengths, provide natural alternative platforms. Operation in this spectral range could enable hybrid nonlinear optical schemes linking x-ray and visible photons, benefiting from the well-developed manipulation and detection techniques available in the visible domain.

In conclusion, we show that hard-x-ray emission can be controlled by coupling SPDC to dispersion-engineered ultraviolet SPPs supported by a multilayer structure. By tailoring the SPP dispersion, the phase-matching landscape is reshaped, imprinting a tunable angular-spectral structure on the emitted x-ray signal. Because the emission properties are governed by phase matching and dispersion, they are determined by the geometry and material parameters of the stack and can be tuned through experimental parameters such as the pump incidence angle or the idler energy. The sensitivity of the SPP dispersion to the dielectric environment further enables dynamic control, for example, through carrier injection [16], external bias [17], or strain [18].

Funding. Israel Science Foundation (2208/24).

Disclosures. The authors declare no conflicts of interest.

Data availability. No data were generated or analyzed in the presented research.

Supplemental document. See Supplement 1 for supporting content.

REFERENCES

1. I. S. Amiri, S. R. Bin Azzuhri, M. A. Jalil, *et al.*, Micromachines **9**, 452 (2018).
2. H. Yu, Y. Peng, Y. Yang, *et al.*, npj Comput. Mater. **5**, 1 (2019).
3. H. Aknin, O. Sefi, D. Borodin, *et al.*, Phys. Rev. Res. **7**, 043226 (2025).
4. E. Sendonaris, J. Sloan, N. Rivera, *et al.*, Optica **12**, 1975 (2025).
5. D. Borodin, S. Levy, and S. Shwartz, Appl. Phys. Lett. **110**, 131101 (2017).
6. D. Borodin, A. Schori, J. P. Rueff, *et al.*, Phys. Rev. Lett. **122**, 023902 (2019).
7. A. Schori, C. Bömer, D. Borodin, *et al.*, Phys. Rev. Lett. **119**, 253902 (2017).
8. S. Sofer, O. Sefi, E. Strizhevsky, *et al.*, Nat. Commun. 2019. **10**, 1 (2019).
9. S. Sofer, O. Sefi, A. G. A. Nisbet, *et al.*, Phys. Rev. B **104**, 085207 (2021).
10. K. Tamasaku and T. Ishikawa, Phys. Rev. Lett. **98**, 244801 (2007).
11. K. Tamasaku, K. Sawada, and T. Ishikawa, Phys. Rev. Lett. **103**, 254801 (2009).
12. K. Tamasaku, K. Sawada, E. Nishibori, *et al.*, Nat. Phys. **7**, 705 (2011).
13. S. Scheel and S. Y. Buhmann, "Macroscopic QED–concepts and applications," arXiv (2008).
14. N. Rivera and I. Kaminer, Nat. Rev. Phys. **2**, 538 (2020).
15. T. E. Glover, D. M. Fritz, M. Cammarata, *et al.*, Nature **488**, 603 (2012).
16. E. Feigenbaum, K. Diest, and H. A. Atwater, Nano Lett. **10**, 2111 (2010).
17. M. Liu, X. Yin, E. Ulin-Avila, *et al.*, Nature **474**, 64 (2011).
18. R. Biele, E. Flores, J. R. Ares, *et al.*, Nano Res. **11**, 225 (2018).